ABSTRACT

CHOCKALINGAM, SEKKAPPAN. Fabrication of Bioinspired Micro/Nano Topography Surfaces through Scalable Roll Coating Process. (Under the direction of Dr. Jong Eun Ryu)

Bioinspired Micro/Nano textured rough topography of a surface has many applications in super-hydrophobicity, self-cleaning surface, anti-icing coatings, anti-biofouling, and drag reduction surfaces. The role of hierarchical and complex surface topography in nature is to amplify the hydrophobicity and maximize the fouling resistance. While there are various manufacture methods to produce these rough topography surfaces, there are still overarching challenges including the cost and manufacturing scalability attributed to the photolithography-based microfabrication processes. Thus, a similar micro- and nano-scale 3-D topographic surfaces inspired from the nature were fabricated using a simple and scalable process.

In this study, we utilized an inexpensive and scalable sheet-to-sheet roll coating method to produce a durable surface based on the carbon nanotube reinforced polymer nanocomposite. The surface textures consisting of micro and nano-scale hierarchical structures were produced due to the transverse instabilities of the non-Newtonian viscoelastic polymer fluid called ribbing. This ribbing instability produces a three-dimensional wavy deformation during the shearing between the rollers. The polymer composite retains the deformed shape due to the recovery of high-viscosity after removing the shear stress.

The nanocomposite material used in this study was synthesized by dispersing 10 wt % of multiwalled carbon nanotube (MWCNT, 10-nm diameter, and 100-μm length) in polydimethylsiloxane (PDMS) polymer. This non-Newtonian viscoelastic paste was mixed initially through the centrifugal planetary mixer. To ensure effective dispersion and homogenisation of the highly entangled MWCNTs within the polymer matrix, a three-roll milling machine was used to perform the mixing for about 30 mins.

The rheology properties of the CNT-PDMS composite pastes, such as the apparent viscosity, was measured by a temperature-controlled rotational rheometer in parallel plate geometry. It was found that this viscoelastic paste polymer followed a shear-thinning behaviour. This behaviour along with the large yield stress acting on the surface of the polymer during shearing between the rollers allowed the formation of ribbing instability. Even after removing this shear stress, the deformed shape was retained due to the recovery of high viscous non-Newtonian paste. Large yield shear stress of the polymer composite makes the composite behaves like a solid in absence of shear stress.

The 3D and 2D surface profiles were instantly characterized by the non-contacting laser scanning confocal microscope (Keyence VK-X1100, 0.5 nm height resolution, and 1 nm width resolution). Detailed surface features were further analysed by the Scanning Electron Microscope. The relationship between the process conditions and the textured structure were studied with the shear rate, capillary number and the surface roughness parameters (e.g., Wenzel factor and density of peaks).

Shear rate is defined as the ratio between the difference between two roll velocities and the gap between the rollers, $\eta=\Delta V/h$. The capillary number is defined as, Ca = viscosity x fluid velocity/surface tension. The results showed that the samples' Wenzel roughness factor increased with the increase in shear rate up to a particular value and then decreased. Similarly, the density of peaks in the sample increased with an increase in capillary number up to a particular value and then decreased. These bioinspired surfaces with hierarchical textured patterns produced using two roll coating process show a tremendous potentiality to be used in super-hydrophobic, anti-biofouling, and drag reduction applications.

Fabrication of Bioinspired Micro/Nano Topography Surfaces through Scalable Roll Coating Process

by
Sekkappan Chockalingam

A thesis submitted to the Graduate Faculty of
North Carolina State University
in partial fulfillment of the
requirements for the degree of
Master of Science

Mechanical Engineering

Raleigh, North Carolina

2021

APPROVED BY:

_____	_____
Dr. Jong Eun Ryu Committee Chair	Dr. Mohammed Zikry
_____	
Dr. Yong Zhu	

DEDICATION

This thesis is dedicated to my always loving and supportive mother, Uma C and father, Chockalingam S for being my backbone throughout my journey. I'd also like to dedicate this to all the people who have supported me throughout my education and made me see this insightful journey through to the end.

BIOGRAPHY

Sekkappan Chockalingam graduated with his bachelor's degree in Mechanical Engineering on May 2019 from Anna University, Chennai, Tamil Nadu. In Fall 2019, he joined NC State University to pursue his Master of Science degree in Mechanical Engineering. He began his research under Dr. Jong Ryu at Composite Design and Manufacturing Laboratory on thin film roll coating surfaces. His research work has been published in IMECE - 2021, ASME conference. His other interests include cricket and politics.

ACKNOWLEDGMENTS

Firstly, I would like to thank my advisor, Dr. Jong Eun Ryu, for all the guidance and encouragement he gave me in the past 2 years. I've grown personally and professionally after joining his lab. He helped me realize my own potential and perform at a higher level than I thought possible. He was a great advisor on and off research. Without his guidance and support this research outcome is definitely not possible.

Next, I would like to thank the members of the committee, Dr. Mohammed Zikry and Dr. Yong Zhu for taking an interest in my research and investing the time to review and improve upon my work.

I would like to thank my research group members, especially Didar and Sipan, who have been great resources and even better friends. One could not hope for better lab mates. Thanks for all the friendly advice and rides you both gave me in the past 2 years.

Finally, a big thanks my parents, Uma C and Chockalingam S, and my sister Ashika C. Without their support I would not have been able to finish this work. They always encouraged me to pursue my education and realize my goals whatever it is. Special thanks to my besties Manisha, Arvind and Bhavana for their support and love at home away from home. A final thanks to all friends who supported me from all parts of the world. Without all of you this would not have been possible.

TABLE OF CONTENTS

LIST OF TABLES vii

LIST OF FIGURES viii

Chapter 1: Introduction 1

1.1 Motivation 1

1.2 Research Gap 2

1.3 Objective 3

Chapter 2: Background 4

2.1 Bioinspired Surfaces 4

2.2 Micro/Nano Textured Surfaces 6

2.2.1 Superhydrophobicity 6

2.2.2 Self Cleaning Surfaces 7

2.2.3 Antibiofouling 8

2.2.4 Drag Reduction Surfaces 9

2.3 Photolithography 10

2.4 Forward Roll Coating Process 12

2.5 Ribbing Instability 14

Chapter 3: Methods and Experiments 19

3.1 Composite Paste Preparation 19

3.2 Two Roll Coating Experiment 19

3.3 Rheology Experiment 21

3.4 Surface Roughness Measurement 21

3.5 Water Contact Angle Measurement 22

3.6 Surface Roughness Descriptors 22

Chapter 4: Results and Discussion 24

4.1 Rheology Property of the Paste 24

4.2 Surface Energy Measurement 26

4.3 Preliminary Results 26

4.4 Experimental Design 28

4.5 Surface Morphology Results 29

4.6 Surface Roughness Results 30

4.7 Effect of Viscosity 33

4.8 Water Contact Angle Results 33

Chapter 5: Conclusions 35

Chapter 6: Future Scope 36

References 37

LIST OF TABLES

Table 2.1: Functional application of natural surfaces 4

Table 4.1: Surface morphology of preliminary experiments 27

Table 4.2: Process parameters of the fabricated samples 29

Table 4.3: Roughness and Water contact angle results of the samples 31

LIST OF FIGURES

Figure 2.1: Natural micro/nano textured surfaces of plants and insects 5

Figure 2.2: Different states of superhydrophobicity 7

Figure 2.3 Schematic of self-cleaning surfaces 7

Figure 2.4: Schematic of antibiofouling mechanism 9

Figure 2.5: Drag Reduction Mechanism 10

Figure 2.6: Schematic of photolithography process 11

Figure 2.:7 Deep reactive ion etching process 11

Figure 2.8: Forward roll coating process 12

Figure 2.9: Meniscus of the fluid between the rollers 13

Figure 2.10: Ribbing instability on the surface of the fluid 13

Figure 2.11: Occurrence of ribbing instability 15

Figure 2.12: Finger like ribbing instabilities 15

Figure 2.13: Forward roll coating setup 16

Figure 2.14: Capillary number vs dimensionless gap ratio 17

Figure 3.1: Schematic of two-roll coating machine with capillary bridging effect 19

Figure 3.2: Process flow of the two-roll coating experiment 20

Figure 3.3: Laser confocal scanned image of the surface 23

Figure 4.1: Viscosity vs shear rate 24

Figure 4.2: G', G" vs oscillation stain 24

Figure 4.3: G', G" vs Frequency 25

Figure 4.4: Parameter plot to finalize process window 28

Figure 4.5: Surface morphology of the12 samples 30

Figure 4.6: Variation of surface descriptors with respect to capillary number..... 31

Figure 4.7: Variation of surface descriptors with respect to shear rate 32

Figure 4.8: Water contact angle results..... 34

Figure 4.9: Variation of water contact angle with respect to capillary number and shear rate ... 34

CHAPTER 1: INTRODUCTION

1.1 Motivation

Micro/Nano textured rough topography of a surface has many applications in super-hydrophobicity, self-cleaning surface, anti-icing coatings, anti-biofouling, and drag reduction surfaces [1]. The surfaces of some living organisms like plant leaves and insects [2,3] consist of micro and nanoscale hierarchical structures. After evolving for billions of years, these organisms have attained an optimum state to survive and handle their habitat better. Acquiring knowledge into how these organisms behave in nature will consistently help researchers wanting to mimic it.

While there are various manufacturing methods to produce these rough topography surfaces, there are still overarching challenges including the cost, manufacturing scalability and durability attributed to the photolithography-based microfabrication processes. Microlithography, the most common method for producing such surfaces, is limited to small area substrates [4]. But for most of the applications of the micro/nano textured surfaces, a large-scale sample is required to fulfil its needs. For example, in a marine drag reduction application, the rough textured surface must cover the whole of the ship hull for it to be effectively used as a drag reduction surface. Thus, a large-scale rough topography surface is very essential.

Considering the complexity and the scalability of the current manufacturing methods of these rough textured surfaces, a new alternative which is simple and can produce large samples was the need of the hour. Thus, the motivation of this study is to manufacture a three-dimensional rough texture surfaces through a simple, inexpensive and scalable process. From literatures it was found that the forward roll coating process is a very simple process to coat materials or fluids on a substrate [4,5]. This process is easily scalable and can produce huge surface area samples. This roll coating process produces transverse defects called ribbing instabilities which creates rough

textures which are three dimensional in nature on the surface of the coatings. These ribbing instabilities are associated with the shearing of non-Newtonian fluids between two rollers.

These instabilities of the roll coating process which are complex hierarchical structures can be exploited and used to our advantage to manufacture a three-dimensional rough texture surfaces through a process which is quite simple and scalable. Thus, the absolute motivation of this research work is to utilize these defects in the roll coating process to manufacture a rough textured surface which is easily scalable and effectively used in its respective applications.

1.2 Research Gap

Many research publications including P. H. Gaskell et al. [6] and E. Szczurek et al. [7] mentioned and documented the transverse defect also called as ribbing instabilities in their research work but none of them tried to exploit and utilize these defects in their potential applications.

Other researchers like C. H. Choi et al. [8] who fabricated micro/ nano textured surfaces never tried to utilize a process which can be scaled for a large surface area to potentially be used in their respective real-world applications.

Some research works similar to the one from S. H. Park et al. [9] reported the fabrication of rough surfaces but didn't study the effect of process parameters on the topology of the surface. It is very essential to obtain the optimum process parameters and design both the process and the paste used in this method to optimize and predict the surface topology. With very limited literatures available in this field, the process parameters were designed based on a preliminary study for it to be efficiently used in their applications.

1.3 Objective

The roll coating process is inexpensive and scalable, and has great potential in manufacturing three-dimensional rough topography surfaces. The main objective of this research

study is to utilize this process to mimic complex surface textures [10] similar to the surfaces of plants and animals consisting micro and nanoscale hierarchical structures.

The manufactured rough topography surface should be durable and possess rough textured surface which are good enough to be used in their potential applications. The roughness of the surface should be quantified effectively and related back to the process parameter to obtain a correlation. The optimum process parameter set to fabricate micro/ nano textured rough surface should be obtained. The correlation results are validated using the water contact angle results which describes the rough topography of the surface.

CHAPTER 2: BACKGROUND

2.1 Bioinspired Surfaces

The surfaces of living organisms like plant leaves and insects, especially on lotus leaves [2] and insect wings [3], consist of micro and nanoscale hierarchical structures. The role of hierarchical and complex surface topography in nature is to amplifies the hydrophobicity and maximize fouling resistance. The enormous diversity of plants and animals in function, texture, size, and shape has always fascinated researchers and scientists. Of the existing 10 million species approximately, many has optimized great technical solutions to respond to their particular environmental conditions. The results of millions of years of biological evolution of millions of species are freely available to scientists that begin to look to biologically inspired solutions for technical products.

The unique properties of biological microstructures bring some interesting findings which are used for active research in the fabrication of the superhydrophobic surface. Mimicking the properties of the multifunctional biological structures is called biomimetics, which inspires the designing and fabricating of various devices and materials for human beings.

Table 2.1: Functional applications of natural surfaces.

Natural Surfaces	Functional Applications
Lotus leaf	Superhydrophobicity, self-cleaning
Water strider leg	Superhydrophobicity, fluid drag reduction
Fish scale, Shark skin	Superoleophobicity/Fluid drag reduction
Butterfly wing	Antireflection, antifogging
Rice leaf, Cactus stems	Superhydrophobicity

The living organisms use the micro/nano topography surfaces to adjust, communicate, and exist in their environments. Self-cleaning, adhesion, bacteriostatic action and superhydrophobicity are some of the main characteristics showed due to their surface chemistry and surface structures at the microscale and nanoscale [11]. Table 2.1 lists the natural surfaces which contains micro/nano textures and their functional applications. The clean surface of the lotus leaf and dragonfly wings can also be attributed to the nano-textures on the surface [12]. These rough textured surface help water striders to travel on the surface of the water with higher speed. The surface topography of the fish scale and shark skin help them to repel water to reduce the drag while moving.

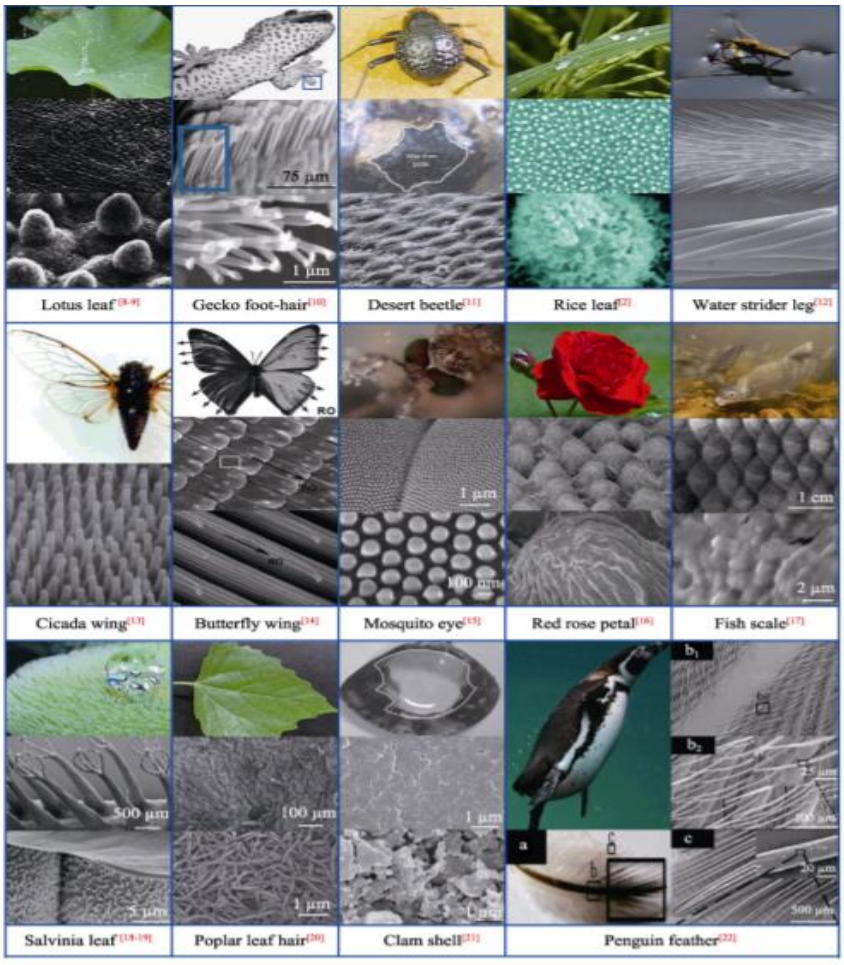

Tong Wei et al., Journal of Inorganic Materials, 2019, 34(11): 1133-1144

Figure 2.1: Natural micro/nano textured surfaces of plants and insects.

Figure 2.1 elaborately shows the natural surfaces of many plants and insects in the environment which contains micro/nano textured surfaces in them [13]. Various plant leaves, flowers and insect wings and legs exhibit a low adhesion, self-cleaning property. This property is termed as the lotus leaf effect, in which water rolls off the surface and removes dust particles. This property is not only seen in biological structures but also stimulates research on the development of artificial superhydrophobic surfaces. The self-cleaning property of a surface can be defined as superhydrophobicity, which is a combination of special hierarchical structures and low surface energy with a high contact angle. After evolving for billions of years, these organisms have attained an optimum state to survive and handle their habitat better. Acquiring knowledge into how these organisms behave in nature will consistently help researchers wanting to mimic it.

2.2 Micro/Nano Textured Surface

Micro/Nano textured rough topography of a surface has many applications in super-hydrophobicity, self-cleaning surface, anti-icing coatings, anti-biofouling, and drag reduction surfaces. These surfaces are inspired from the nature. All of the applications of such rough hierarchical textured surfaces are explained in the below sections.

2.2.1 Superhydrophobicity

Superhydrophobic surfaces are surfaces with a water contact angle (WCA) above 150° and a hysteresis angle lower than 5°. Superhydrophobicity is defined as a surface having a water advancing angle $\theta A \geq 145°$ and receding angle $\theta R > 90°$ [14]. When the liquid is in intimate contact with the microstructured rough surface, then the surface is present in the Wenzel region as shown in Figure 2.2. When there is small protrusion like textures on any surface, the spacings cannot be occupied by the liquid and therefore be filled with air. In this case, the wettability of that surface enters the Cassie-Baxter regime. In this regime, the WCA depends on the area of the surface that

is in contact with the liquid. Hence surface topography has an extreme effect on the wettability of the material surface. Non-wettable surfaces are composed of close-packing molecules which has a relatively low surface energy.

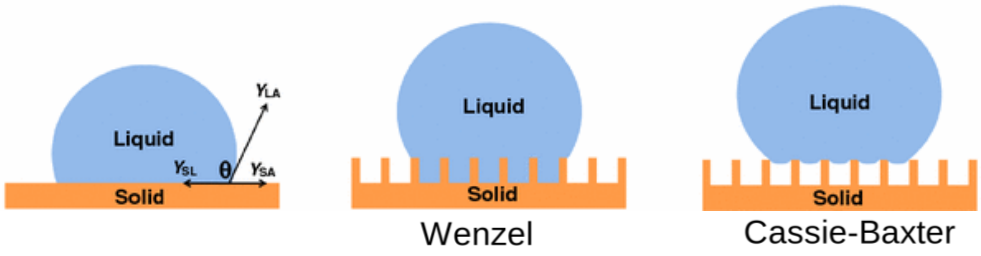

Zhang, D., et al. J Coat Technol Res 13, 11–29 (2016)

Figure 2.2: Different states of superhydrophobicity.

2.2.2 Self Cleaning Surfaces

Lotus leaves in nature always has a clean appearance in spite of growing in a dusty environment, because the water droplets roll off the leaves immediately upon contact with the leaf due to the superhydrophocity of the leaves as mentioned earlier. This carries away the dirt present on its surface with it at the same time. This promising self-cleaning property have triggered research interest in the development of artificial superhydrophobic surfaces towards dirt-resistant applications.

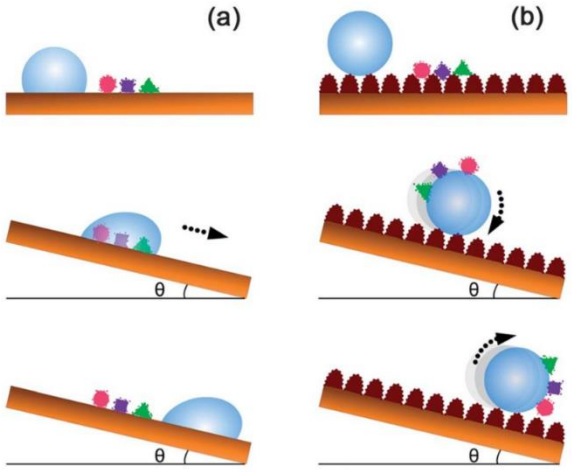

Zhang, Y.-L et al., (2012), Soft Matter, 8(44), 11217

Figure 2.3 Schematic of self-cleaning surfaces.

Figure 2.3 shows the concept of the self-cleaning behavior of a superhydrophobic surface. When compared with a normal surface, the water droplet on a superhydrophobic surface shows a quasi-spherical shape. When it is tilted to a certain angle, the water droplet rolls off the surface easily and picks up foreign dirt particles on the surface at the same time, this is considering the fact that most dust shows relatively strong adherence to water in comparison to a solid surface. In this way, superhydrophobic surfaces can keep their surfaces clean. Typically, when the sliding angle of a superhydrophobic surface is lower than 10°, it means that the surface has self-cleaning properties [1]. K.Y. Law [14] in his research paper showed that the key enabler for self-cleaning is surface slipperiness, not the large static contact angle as many suggested. Further investigation reveals that the main contributor to surface slipperiness is the small contact angle hysteresis.

2.2.3 Antibiofouling

The biofouling is defined as the accumulation of living organisms on the surface including bacteria, fungi, protozoa, algae and invertebrates. The major economic problem for many marine industries lies in the settlement of marine organisms on parts of their submerged surfaces. Anti-fouling is the process of preventing these accumulations from forming. These organisms are killed or repelled from the surface with the help of the wettability and surface texture of the surface used. The settlement and adhesion of the organisms to surfaces are studied through the biofouling experiments.

Schumacher et al. [15], reported the results of the experiments designed to evaluate the effect of topographic feature size, geometry, and roughness on settlement of Ulva zoospores. Nano-textured surfaces kill bacteria because surfaces with bed of nails destroys bacteria through puncturing the cell wall. Once the bacteria land on the surface, they are subjected to adhesive forces. These can deform the bacterial membrane, but by themselves, do not cause the bacteria to

rupture. When they do move, shear forces pull on the polymeric substance, ripping the membrane apart. This provides the explanation why rough textured surface acts as an antibiofouling surface.

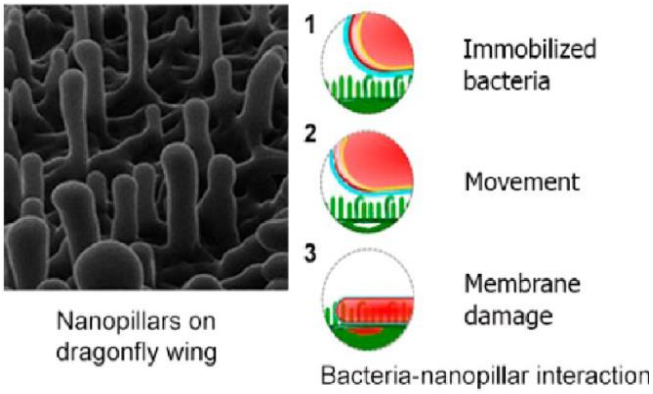

Bandara et al., ACS Appl. Mater. Interfaces 2017, 9, 6746−6760

Figure 2.4: Schematic of antibiofouling mechanism.

Figure 2.4 shows the schematic of the antibiofouling mechanism. Reversible bacterial adhesion is operationally defined here as a situation in which a bacterium remains very close to a surface for a period of several minutes. Reversibly adhering bacteria are presumed to retain their ability to move laterally along the surface by swimming or Brownian motion. In irreversible adhesion, by contrast, bacteria adhering to the surface do not move, either by swimming or Brownian motion, for the duration of observation. In general, bacteria that have become immobilized on the surface are described as irreversibly adhered to the surface, while cells that can still swim along the surface are described as reversibly adhered. It would be advantageous to control cellular adhesion and prevent formation of harmful biofilms before they start.

2.2.4 Drag Reduction Surfaces

One of the major applications of superhydrophobicity is it's drag reduction performance [16]. Figure 2.5 shows the drag reduction mechanism. The hydrophobic surface created by a polymer coating is irregularly rough and the fine grooves i.e., cracks formed on the rough surface are random in size and pattern, making it difficult to isolate the effect of trapped air and to utilize the effective slip in a controllable manner. The slip length is defined as the distance from the crest

of the nanograting surface to the depth at which the linearly extrapolated liquid velocity reaches zero. The large slip over the hydrophobic nanograting surfaces indicates that their effective slip was caused by the nanostrips of air in the troughs (Cassie-Baxter). An important consequence of the surface slip is the reduction of drag or pressure drop. This helps in reducing the drag force and improving the fluid speed over the surface.

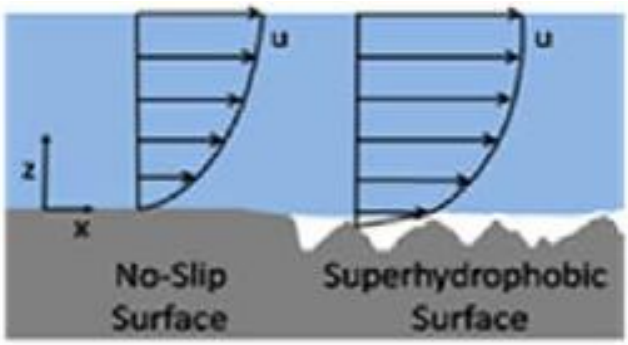

Park, S.-H. et al., Sci. Rep. 5, 15430; (2015)

Figure 2.5: Drag Reduction Mechanism.

2.3 Photolithography

There are various manufacturing methods to produce these rough topography surfaces. But there are still overarching challenges including the cost, manufacturing scalability and durability attributed to the photolithography-based microfabrication processes. Photolithography is the most common method for producing such surfaces. Figure 2.6 shows the schematic of the photolithography process.

Photolithography is a process used in microfabrication to pattern parts on a thin film or the bulk of a substrate. It uses light to transfer a geometric pattern from a photomask to a photosensitive i.e., light sensitive chemical photoresist on the substrate. A series of chemical treatments then either etches the exposure pattern into the material or enables deposition of a new material in the desired pattern upon the material underneath the photoresist.

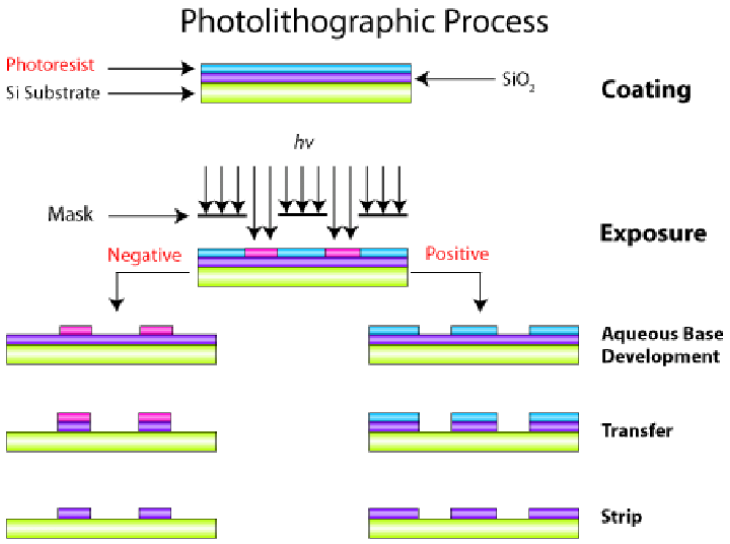

Figure 2.6: Schematic of photolithography process.

The basic procedure or process sequence of this process is as follows: cleaning, substrate preparation, photoresist application, align photomask, exposure to UV lights, development and removal of photoresist exposed to UV light, etching of the surface and photoresist removal. Etching which is the main process in patterning is majorly done through the deep reactive ion etching (DRIE) process as shown in Figure 2.7.

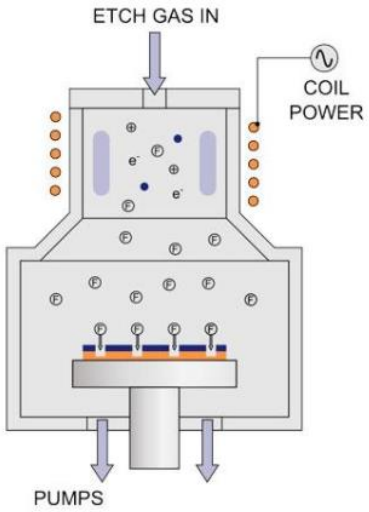

Figure 2.7: Deep reactive ion etching process.

In this process, the patterned photoresist is used as the etching mask. The accelerated plasma ions inside the chamber react with the surface of the substrate and knock the atoms out of the material to form the pattern. Alternate plasma etches and passivation modes are used since the passivation protects sides of trench. This helps in attaining high aspect ratio patterns.

The main limitation of such surface is the scalability of this process. It's limited to small area substrates [4]. Thus, new processes which is inexpensive and scalable is required.

2.4 Forward Roll Coating Process

The roll coating is extensively used in the paint and coating industry. The aim of the roll coating is to apply a thin liquid film on a moving substrate. Figure 2.8 shows the basic schematic of the roll coating process. It consists of two rollers rotating in opposite direction to coat the fluid on one of the rollers. The roll coating permits a high continuous speed and less defects application in theory. But in reality, a transverse defect appears.

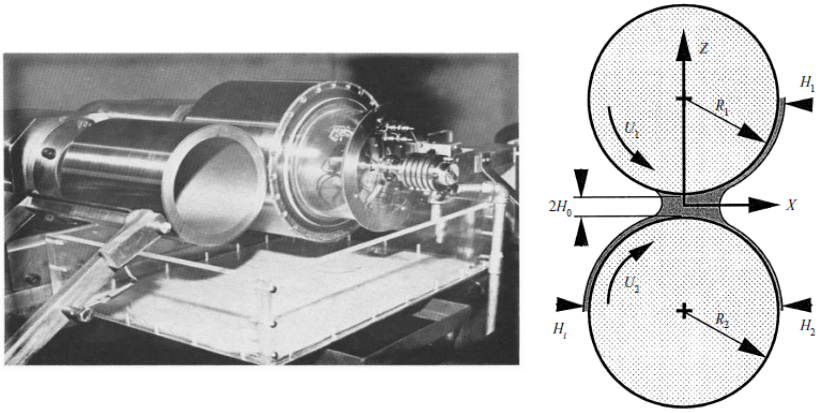

P. H. Gaskell et al., J. Fluid Mech. (1998), vol. 355, 17-44

Figure 2.8: Forward roll coating process.

This defect is commonly called "ribbing" and is characterized by periodic ribs parallel to the moving direction of the substrate. Roll coating is widely used to apply a thin liquid layer to a continuous, flexible substrate. At low speeds the flow is two dimensional and steady; as the roll speed is raised, the two-dimensional flow becomes unstable and is replaced by a steady three-dimensional flow which results in more or less regular stripes in the machine direction. This type

of instability, or rather the three-dimensional flow to which it may lead, is commonly called ribbing.

E. Szczurek et al., Journal of materials processing technology, 20 (2009), 3187–3197

Figure 2.9: Meniscus of the fluid between the rollers.

Figure 2.9 shows the mechanics of the meniscus during roll coating. The flow patterns revealed are seen to consist of large two-dimensional re-circulations extending throughout the coating bead. This forms the transverse defects called ribbing as mentioned earlier. A clear view of the ribbing instability on the surface after the coating process is completed is shown in Figure 2.10.

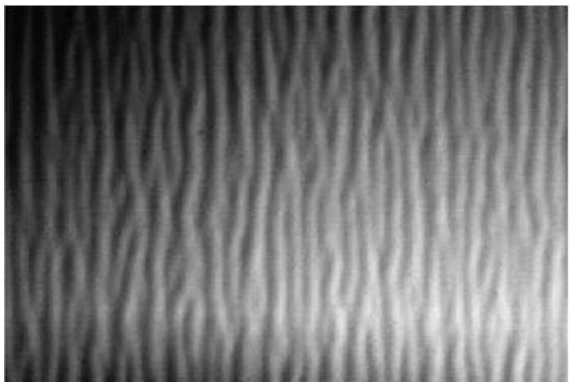

E. Szczurek et al., Journal of materials processing technology, 20 (2009), 3187–3197

Figure 2.10: Ribbing instability on the surface of the fluid.

Park et al. [9] fabricated superhydrophobic surfaces through simple and scalable roll-to-roll processing. They used high viscosity of the nanotube/elastomer paste for the fabrication. A double-roll based process was used to fabricate the SH film. At a certain V_2/V_1 ratio (> 1), a randomly structured pattern develops over the entire film area (V_2 – velocity of roll 2, V_1 – velocity of roll 1). The effective shear rate $\eta = \Delta V/h$, where $\Delta V = V_1 - V_2$ and h is the thickness of film. A smooth film without any patterning was formed when $\eta > 0\ s^{-1}$ (e.g., for $\eta = 32\ s^{-1}$, $V_1 > V_2$) and irregular surface morphologies was formed when $\eta < 0\ s^{-1}$ and the hydrophobicity was decreased after $\eta < -82\ s^{-1}$. They used Fields Newtonian model to find the wavelength but they have used a non-Newtonian fluid. They conclude that there may be significant differences between the velocity profile modeled for Fields Newtonian model and that of the non-Newtonian MWCNT/PDMS paste used here due to shear-thinning phenomenon.

The surface textures consisting of micro and nano-scale hierarchical structures were produced due to the ribbing instability of the viscoelastic polymer during the shearing between the rollers. Thus, in this study, we utilized an inexpensive and scalable roll-to-roll method to produce a durable surface based on the ribbing instabilities [5, 17] associated with the shearing of non-Newtonian fluids between two rollers.

2.5 Ribbing Instabilities

Fields et al. [5] derived the conditions for the instability to occur, and expressions for the finger spacing and for the overall growth-rate of the finger-like crack. Figure 2.11 shows when the instability in fluid flows start to occur. It occurs when a thin layer of liquid is pulled when it's between two parallel plates or when the plates are puller apart each other when the liquid is present

between the plates or when the liquid is sheared between a roller and a plate. In all of these cases, the cracks or instability grows.

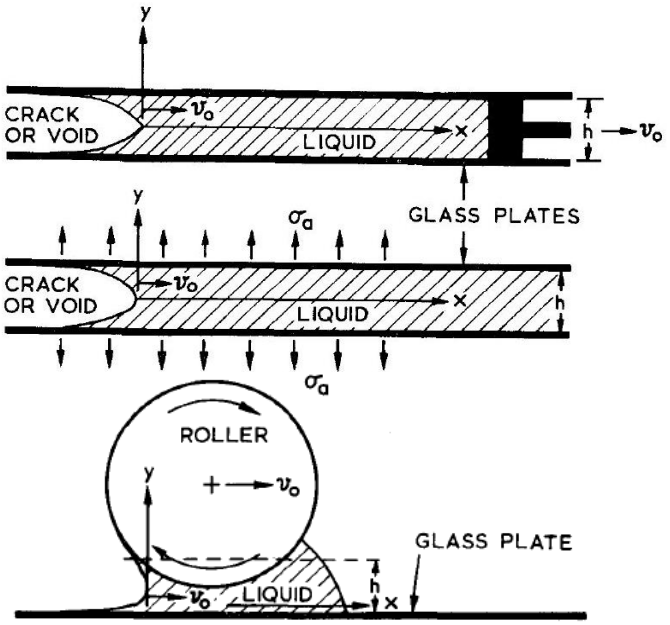

R. J. Fields and M. F. Ashby, Philosophical Magazine, 1976, Vol 33, No. 1, 33-48

Figure 2.11: Occurrence of ribbing instability.

When the separation velocity of the plate or the fluid (v_0) is less (slow rate) or viscosity of the paste is low the crack front or instability shape appears to be smooth and straight as shown in Figure 2.12. As the rate of separation v_0 or the viscosity of the paste increases, the instabilities break down into a finger like structure depicted in Figure 2.12.

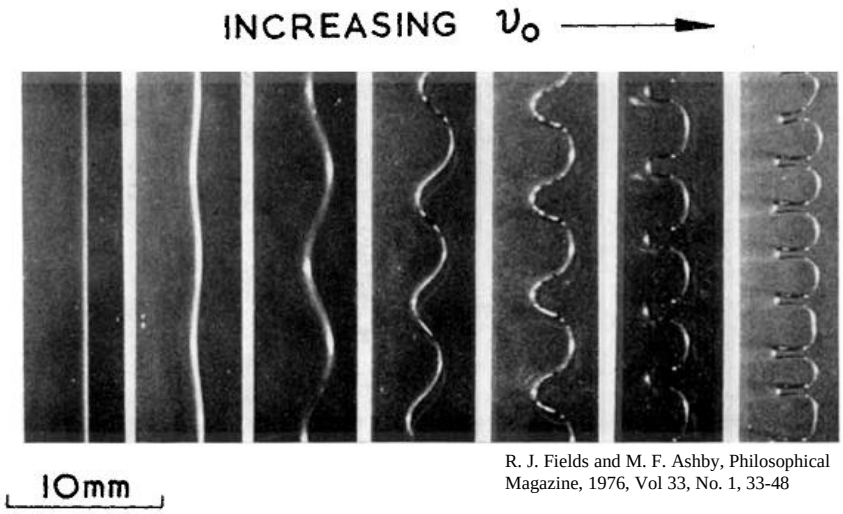

R. J. Fields and M. F. Ashby, Philosophical Magazine, 1976, Vol 33, No. 1, 33-48

Figure 2.12: Finger like ribbing instabilities.

Grillet et al. [17] investigated the strong elastic destabilization of forward roll coating. He found that interfaces which are stable for Newtonian fluids are unstable via purely elastic mechanisms. He studied the onset condition of the fingering instability. It was based on dimensionless critical capillary number (Ca) which is defined as the ratio of viscous to surface tension forces.

$$Ca = \frac{\mu U}{\sigma} \tag{1}$$

where μ is the fluid viscosity, U is the mean flow velocity and σ is the surface tension.

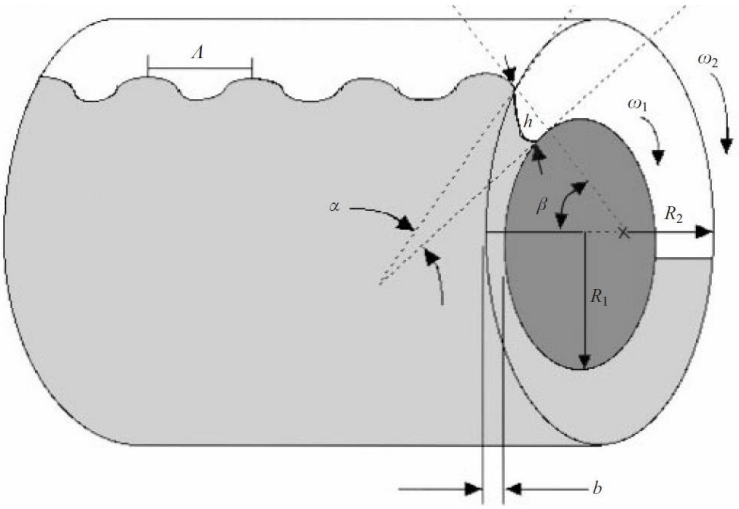

A. M. Grillet et al., J. Fluid Mech. (1999), vol. 399, 49-83

Figure 2.13: Forward roll coating setup.

The critical conditions depend on $\varepsilon^{1/2}$Wi where ε is the ratio of gap width to radius of the cylinder and Wi is the Weissenberg number. The Weissenberg number is defined as,

$$Wi = \frac{U\lambda}{b} \tag{2}$$

where U is the mean flow velocity, λ is relaxation time and b is the gap thickness. Below is the expression for critical condition as suggested by Grillet.

$$Ca/Bo = \mu U/\rho g b2 = G \tag{3}$$

where Bo is bond number and G is the gravity parameter. They used an eccentric cylinder with half full of liquid. Both the cylinder rotates in the same direction (forward) with same angular speed. To get a measure of the elasticity of each Boger fluid, the elastic parameter N is defined as the ratio of the Weissenberg and capillary numbers at the maximum gap width,

$$N = \frac{\lambda U/b}{\mu U/\sigma} = \frac{\lambda \sigma}{\mu b} \qquad (4)$$

They found that over the entire range of dimensional gaps (b/R) examined, where *R* is the mean radius of cylinders, the gravitation stabilization was comparable to or greater than that due to surface tension. Compared critical conditions Ca, G vs b/R and found that the agreement is fairly good over the entire range with the measured critical conditions being about 5-10% above the Saffman-Taylor theory. The results are shown in Figure 2.14.

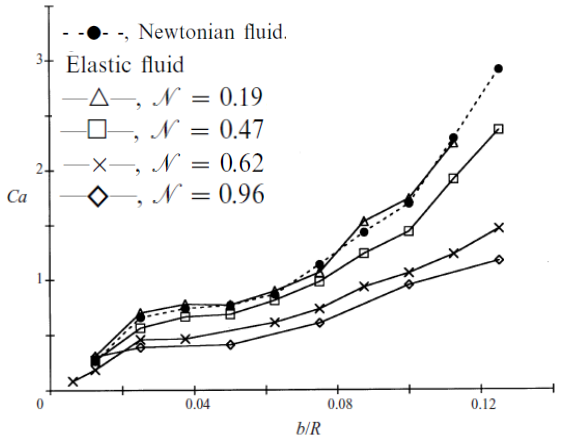

A. M. Grillet et al., J. Fluid Mech. (1999), vol. 399, 49-83

Figure 2.14: Capillary number vs dimensionless gap ratio.

For weak elastic fluid, N= 0.19 there is no measurable change in the critical conditions over the Newtonian fluid flow. However, for the more elastic fluids, N = 0.62 and 0.96 there is a very significant decrease in the elastic critical speed for the onset of instability causing the critical capillary number to fall by a factor of 3 for the largest gap ratios. Similarly for elastic fluids, a strong increase in wavenumber at the critical condition was discovered. Instead of the occasional tip splitting seen in the Newtonian case, the fingers in the elastic fluid were constantly tip splitting

resulting in liquid bridges which produced tree-like structures. Insights from all these literatures were obtained to design the methods and experiments of this research work.

CHAPTER 3: METHODS AND EXPERIMENTS

3.1 Composite Paste Preparation

The nanocomposite material used in this study was synthesized by dispersing 10 wt % of multiwalled carbon nanotube (MWCNT, 10-nm diameter, and 100-µm length) in polydimethylsiloxane (PDMS) polymer. This non-Newtonian viscoelastic paste was mixed initially through the centrifugal planetary mixer. To ensure effective dispersion and homogenisation of the highly entangled MWCNTs within the polymer matrix, a three-roll milling machine was used to perform the mixing for about 30 mins. The composite paste preparation process is depicted in Figure 3.2.

3.2 Two Roll Coating Experiment

A two-roll coating machine was used to fabricate the textured samples. Two rollers with diameter 50.8 mm and length 300 mm were placed parallel to each other and the high viscosity CNT-PDMS polymer composite was placed in between the rollers. The speed of both the rollers can be varied from 0 to 120 rpm and it can be done independently. A schematic of the two-roll coating machine is shown in Figure 3.1.

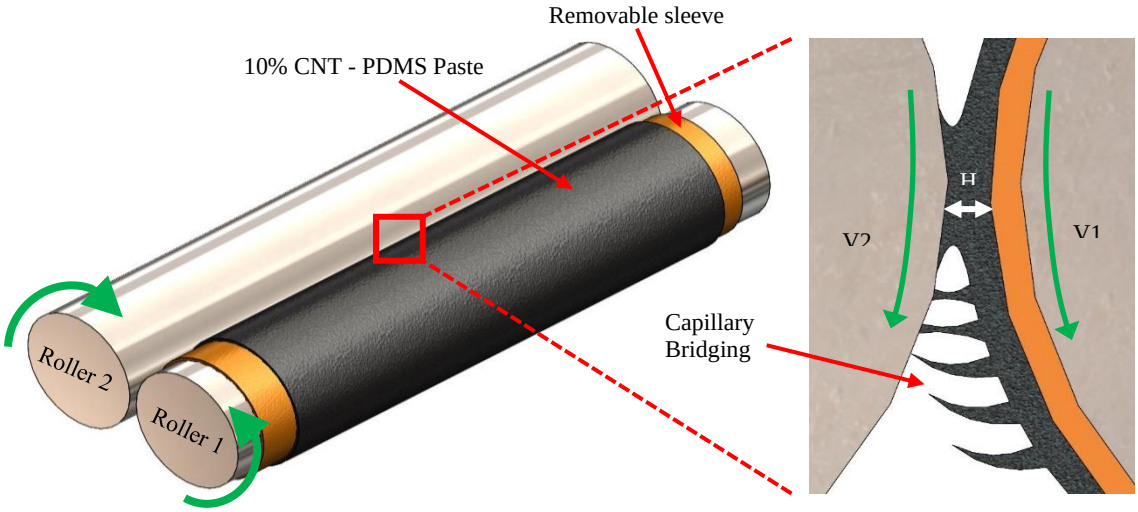

Figure 3.1: Schematic of two-roll coating machine with capillary bridging effect.

Here, V1 is the velocity of roller 1 and V2 is the velocity of roller 2. H is the gap between the rollers. Roller 1 has a removable polyimide sleeve which is used to remove the sample after fabricating it. Once the rollers start to rotate the paste gets transferred onto the roller with the higher speed and is spread across the circumference of the roller as depicted.

In our study, V1 is kept greater than V2 when the paste is inserted. Thus, the paste is coated as a smooth film onto roller 1. Then, V2 is kept constant and V1 is gradually reduced below V2. When V1 is lesser than V2, it was seen that the paste on roller 1 starts to attach and then transfer to roller 2 in the line of contact between the two rollers by a phenomenon called capillary bridging [9] as shown in Figure 3.1.

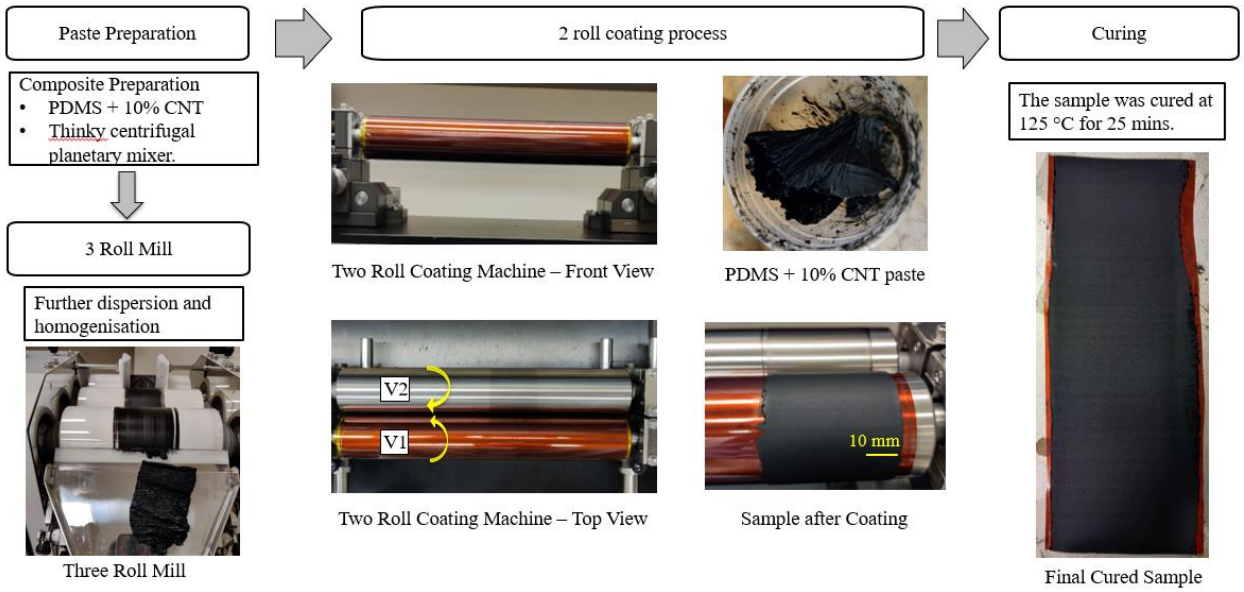

Figure 3.2: Process flow of the two-roll coating experiment.

After coating, the samples were thermally cured at 125 °C for 25 mins in an oven. The complete composite paste preparation and two roll coating experiment is presented in the above process flow chart shown in Figure 3.2.

3.3 Rheology Experiment

The rheology properties of the 10% CNT-PDMS composite paste, such as the apparent viscosity, storage modulus and loss modulus were measured by a temperature-controlled rotational rheometer. The TA Instruments Discovery Hybrid-3 rheometer was used in our experiment. It is a temperature-controlled rotational rheometer used in the parallel plate geometry. The conditions of the experiment are as follows:

- 1000 micron gap height
- 8 mm cross-hatched steel plates
- Temperature 25 $^{\circ}$C
- Amplitude sweep: $5x10^{-3}$ to 5 oscillation strain % @ 1 Hz
- Frequency sweep: 0.03 strain%.

3.4 Surface Roughness Measurement

The 3D and 2D surface profiles were instantly characterized by the non-contacting laser scanning confocal microscope. The Keyence VK-X1100 confocal laser scanning microscope with a 0.5 nm height resolution, and 1 nm width resolution was used. A 20x lens was used to scan the surface of the sample with a total magnification of 480x. The multifile analyser software was used to retrieve the results from the scanned image.

A more detailed surface features and topography were further analyzed by the Scanning Electron Microscope. The Field Emission Scanning Electron Microscope - Verios 460L was used in our study. The resolution of this equipment is 0.6 nm from 2 kV to 30 kV.

3.5 Water Contact Angle Measurement

The water contact angle of the samples was measured using the contact angle goniometer. Water contact angles of the samples were measured in 5 to 8 locations and the average of it was reported.

3.6 Surface Roughness Descriptors

Conventional surface roughness values like R_a, R_q and R_{max} doesn't describe the 3D topography of the surface completely. They offer no insights about the horizontal roughness and its density. Thus, a new surface roughness descriptor was necessary to understand the overall roughness description of any sample. We need better descriptors which takes into account both the 2D and 3D texture of the surface. Two such descriptors used in this study are Wenzel roughness factor (r) and peak density (Spd).

Wenzel roughness factor is defined as the ratio of the Actual (textured) surface area to the cross-section area of the sample.

$$r = \frac{Actual\ Surface\ Area}{Cross\ Section\ Area} \tag{5}$$

The laser confocal Multifile analyzer software gives the Developed Interfacial Area Ratio (Sdr) of the sample. Sdr is defined by as the difference between the Actual textured surface area and the footprint cross section area over the footprint cross section area.

$$Sdr = \frac{Actual\ Surface\ Area - Cross\ Section\ Area}{Cross\ Section\ Area} \tag{6}$$

From this Sdr, the r value can be obtained by adding 1 to it.

$$r = 1 + Sdr \tag{7}$$

So, from the equation it is obvious that a higher value of r means that the roughness of the sample is also higher.

Peak density is the number of peaks in a given area. Here the area is considered as 1 mm^2. Thus, the no. of peaks in 1 mm^2 are is reported as Spd. This value is directly obtained from the Multifile analyzer software. Again, a higher value of Spd means that the roughness of the sample is also higher. An example of the scanned image of the surface from the laser confocal Multifile analyzer software is shown in Figure 3.3.

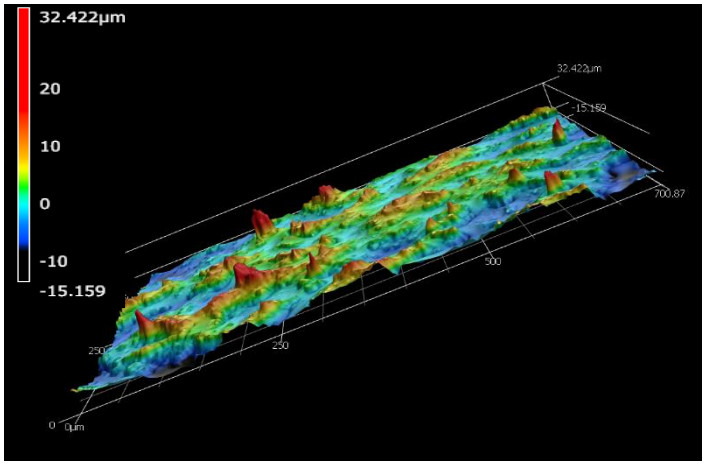

Figure 3.3: Laser confocal scanned image of the surface.

CHAPTER 4: RESULTS AND DISCUSSIONS

4.1 Rheology Property of the Paste

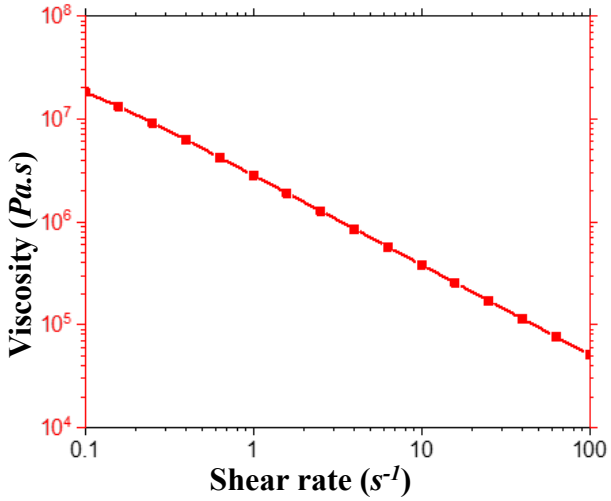

Figure 4.1: Viscosity vs shear rate.

From the Figure 4.1 it was seen that the viscosity of the paste reduces as the shear rate increases. This confirms that the non-Newtonian composite paste followed a shear thinning behavior.

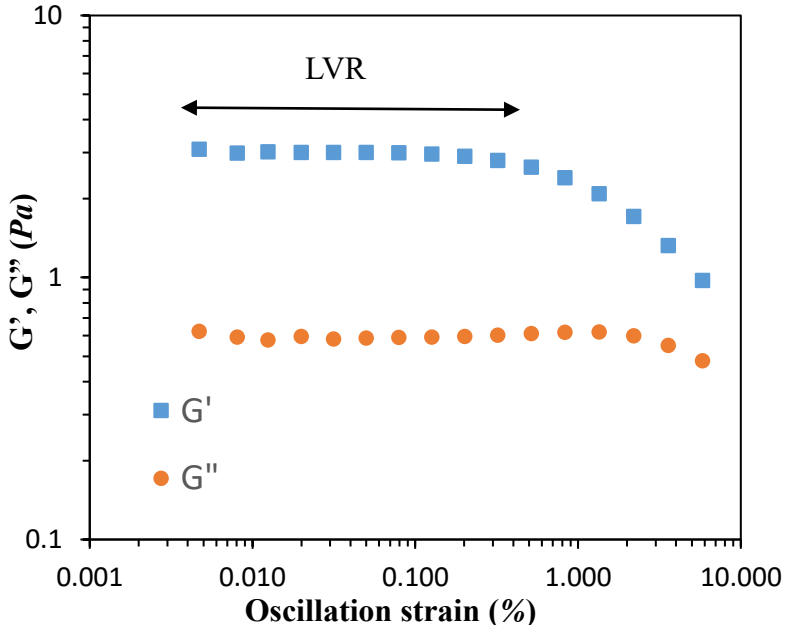

Figure 4.2: G', G" vs oscillation stain.

Storage Modulus (G') is defined as the measure of elasticity of material. This is the ability of the material to store energy. The Loss Modulus (G") is defined as the measure of viscosity of the paste. This is the ability of material to dissipate energy. These moduli were plotted with respect to the oscillatory strain to locate the Linear Viscoelastic Region (LVR). The stable moduli value for a range of oscillatory strain confirms the LVR for the used 10% CNT – PDMS composite paste. It also shows a satisfactory strain resistance before it yields

The viscoelastic behavior at the LVR was presented in the Figure 4.3. Figure 4.3 plots the frequency sweep with respect to the two moduli. It had a very linear trend without any fluctuations. It was also seen that the value of the storage modulus (G') is great than the value of the loss modulus (G"). Thus, the experiment confirmed that the composite paste has an elastic solid like nature.

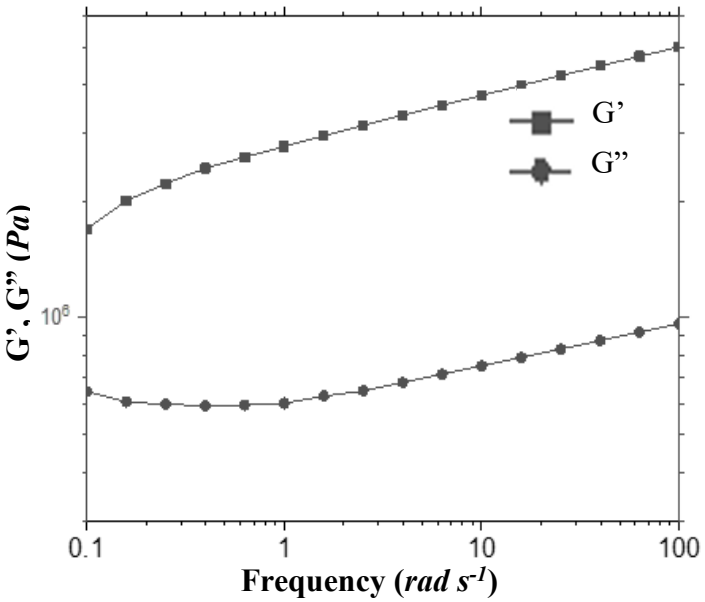

Figure 4.3: G', G" vs Frequency.

4.2 Surface Energy Measurement

The surface energy was measured using the Owens-Wendt Model [18]. Four different test liquids were used to measure the liquid contact angles on the surface. Based on the contact angle results, the Owens-Wendt model was plotted and the surface energy of the solid surface used was measured. From the experiment conducted, the surface energy or the surface tension of our sample was found to be 22.47 mJ/m^2.

4.3 Preliminary Results

A preliminary study was conducted to see how the composite paste behaved in our two-roll coating set up. The roll coating experiment was established and the initial samples were fabricated with various roller speeds. The gap between the rollers were kept constant at 0.5 mm throughout the experiments. To clearly understand the effect of the process speeds and the composite paste property, two parameters were described.

Shear rate is defined as the ratio between the difference between two roller velocities and the gap between the rollers as shown in equation. The capillary number (Ca) is defined as the product of viscosity and fluid velocity over the surface tension.

$$Shear\ rate = \frac{V1-V2}{h} \tag{8}$$

$$Ca = \frac{Viscosity \times Avg.\ Velocity}{Surface\ Tension} \tag{9}$$

The shear rate defines the effect of the process while the capillary number defines the effect of the paste on the two roll coating experiments. Table 4.1 shows the process parameters and the surface morphology of the preliminary results. 6 samples A-F were fabricated in the preliminary study. Sample E was the only sample to show a desired rough textured surface. All other samples

showed a smooth surface. To better understand the results, the process parameters were plotted based on the surface roughness as shown in Figure 4.4.

Table 4.1 Surface morphology of preliminary experiments.

Sample Name	V1 (rpm)	V2 (rpm)	Shear Rate (1/s)	Viscosity (Pa-s) ($x10^5$)	Capillary Number ($x10^5$)	SEM Image
A	43	58	-79.80	0.69	4.28	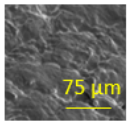
B	33	53	-106.40	0.54	2.84	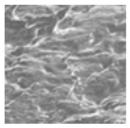
C	33	63	-159.59	0.38	2.24	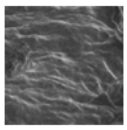
D	20	41	-111.72	0.52	1.93	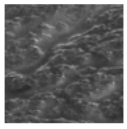
E	33	41	-42.56	1.19	5.38	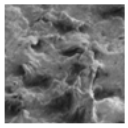
F	26	41	-79.80	0.69	2.84	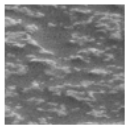

Figure 4.4 shows the parameter plot to finalize the process window to fabricate the samples. The shear rate is plotted with respect to various samples in Figure 4.4 (a). The roughness designation is indicated by different colours. The sample E shows the roughest surface (red) with shear rate of -42.56 s^{-1}. It is seen that shear rate below -80 s^{-1} always produces smooth surfaces only. Also, if the shear rate is very low in magnitude (say -20 s^{-1}), it might not be enough to produce rough surfaces. Thus, we attain an operable range of shear rate of around – 20 s^{-1} to – 80 s^{-1}.

A similar plot was made for the capillary number in Figure 4.4 (b). Sample E, the roughest surface (red) had a capillary number of 5.38 x 10^5. It is seen that surfaces with capillary number

approximately below 4 x 10^5 always produces smooth surfaces only. While we are unaware of the upper limit of this capillary number for attaining the rough surface, it is concluded that it must possess a minimum of this critical capillary number for the rough textures to appear. It is also expected that there is a higher possibility to attain rough surfaces for capillary number greater than 4.5 x 10^5. It should also be noted that to achieve a rough surface, the conditions for both shear rate and capillary number should be satisfied.

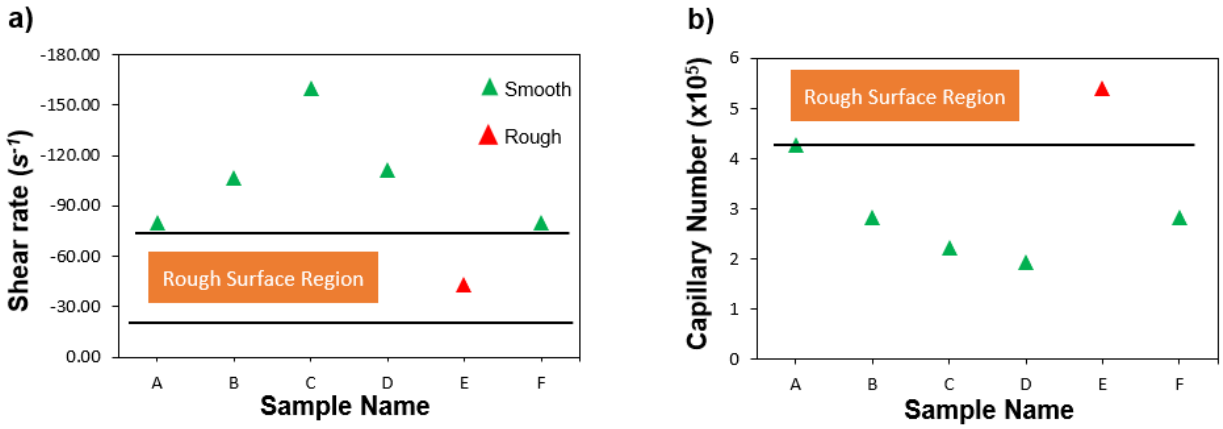

Figure 4.4: Parameter plot to finalize process window.

4.4 Experimental Design

Based on our preliminary study, the parameters were selected from the process window defined. 4 levels of shear rate and 3 levels of capillary number were used to fabricate the samples. Thus, in this study 12 samples were fabricated and analyzed as documented in Table 4.2. For each shear rate, 3 levels of capillary numbers were used.

Table 4.2: Process parameters of the fabricated samples.

Sample Name	V1 (rpm)	V2 (rpm)	V1 (cm/s)	V2 (cm/s)	Shear Rate (s^{-1})	Viscosity ($x10^5$) (Pa-s)	Capillary Number ($x10^5$)
1a	36	41	9.58	10.91	-26.60	1.79	8.39
1b	26	31	6.92	8.25	-26.60	1.79	6.21
1c	16	21	4.26	5.59	-26.60	1.79	4.03
2a	43	51	11.44	13.57	-42.56	1.19	6.83
2b	33	41	8.78	10.91	-42.56	1.19	5.38
2c	23	31	6.12	8.25	-42.56	1.19	3.93
3a	50	61	13.30	16.23	-58.52	0.91	6.14
3b	40	51	10.64	13.57	-58.52	0.91	5.03
3c	30	41	7.98	10.91	-58.52	0.91	3.93
4a	56	71	14.90	18.89	-79.80	0.69	5.38
4b	41	56	10.91	14.90	-79.80	0.69	4.11
4c	26	41	6.92	10.91	-79.80	0.69	2.84

4.5 Surface Morphology Results

At a certain shear rate, a micro/nano structured rough topography develops over the entire film area. The formation of this instability pattern is strongly related to the dynamic rheological property and the process parameters. The resulting pattern, consisting of micro- and nano-scale features resembled the bristled shark skin according to S.H. Park et al [9]. Even after removing this shear stress, the deformed shape was retained due to the recovery of high viscous non-Newtonian paste. Large yield shear stress of the polymer composite makes the composite behaves like a solid in absence of shear stress similar.

Figure 4.5 shows the SEM images of all the 12 samples. A basic understanding of the samples was obtained using these SEM images. It was seen that the medium and high Ca samples were rougher than the low Ca samples. Also, samples with shear rate -42.56 s^{-1} and -58.52 s^{-1}

showed rough surfaces compared to others. However, these images were compared with the surface descriptors obtained using the laser confocal data.

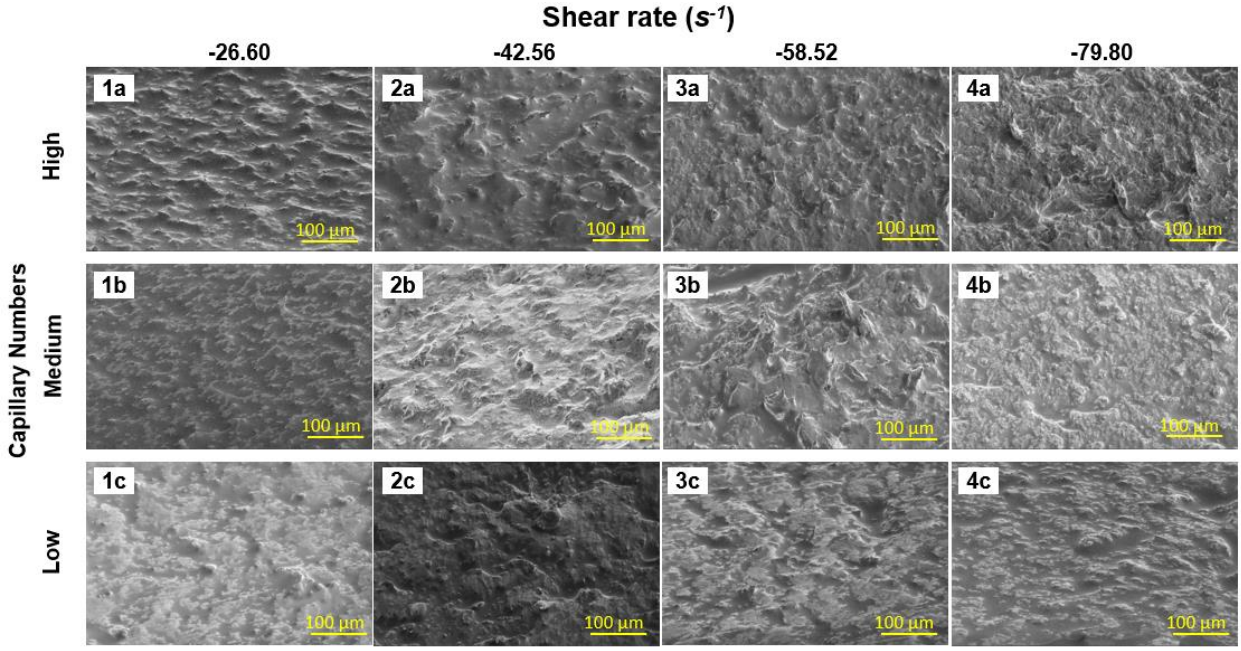

Figure 4.5: Surface morphology of the12 samples.

4.6 Surface Roughness Results

The relationship between the process conditions and the rough textured surface characteristics was studied using the shear rate, capillary number and the surface roughness descriptor. The results from the laser confocal roughness measurement were obtained and document in Table 4.3. The variation in the Wenzel roughness factor (r) with respect to the capillary number for various shear rate was plotted in Figure 4.6 (a). It can be seen that the lowest and highest shear rate had a linear increasing trend. The r of mid shear range (40 - 60 s^{-1}) showed an initial increase and then decreased with increase in Ca.

A sample was considered as a good textured sample if the r value was greater than 1.5. From our results, we found that, for r value to be greater than 1.5, the range of capillary number should be from 4.5 x 10^5 to 6.0 x 10^5 and Shear rate should be greater than 40 s^{-1}. Almost all of

the samples with capillary number around 5 x 10^5 and shear rate was greater than 40 s^{-1} (Sample 2b, 3b, 4a) had high r value. The sample with high roughness and the textured surface was obtained with a shear rate of -42.56 s^{-1} and a capillary number of 5.38 x 10^5. All samples with shear rate greater than 40 s^{-1} have more than 10,000 peaks which guaranteed a minimum textured surface.

Table 4.3: Roughness and Water contact angle results of the samples.

Sample Name	Wenzel Roughness Factor	Peak density (mm^{-2}) ($x10^4$)	Avg. Water Contact Angle (°)
1a	1.236	1.22	118.09
1b	1.054	0.50	116.62
1c	1.051	0.93	116.32
2a	1.324	1.08	118.17
2b	1.913	3.61	123.86
2c	1.483	1.95	119.05
3a	1.393	2.21	122.55
3b	1.891	2.82	126.53
3c	1.238	2.58	119.72
4a	1.817	3.94	127.88
4b	1.375	3.07	123.08
4c	1.153	1.41	119.68

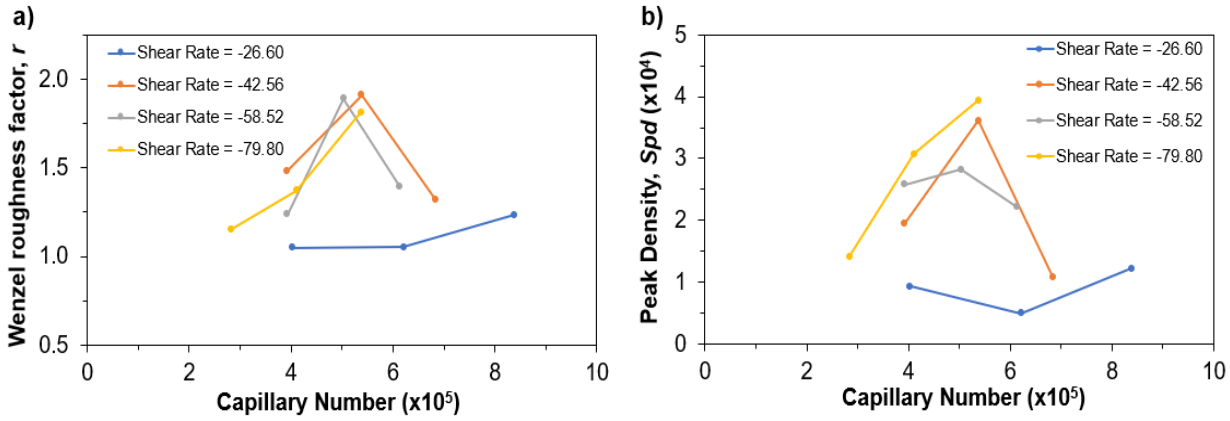

Figure 4.6: Variation of surface descriptors with respect to capillary number.

Figure 4.6 (b) shows the variation of peak density with the capillary number. The samples with mid Ca showed high roughness in terms of no. of peaks. Samples with high capillary number showed an increasing trend, while other samples showed an initial increase in peak density and then decreased. All samples with shear rate greater than 40 s^{-1} have more than 10,000 peaks which guaranteed a minimum textured surface. Sample in mid capillary number region showed higher peak density than other samples.

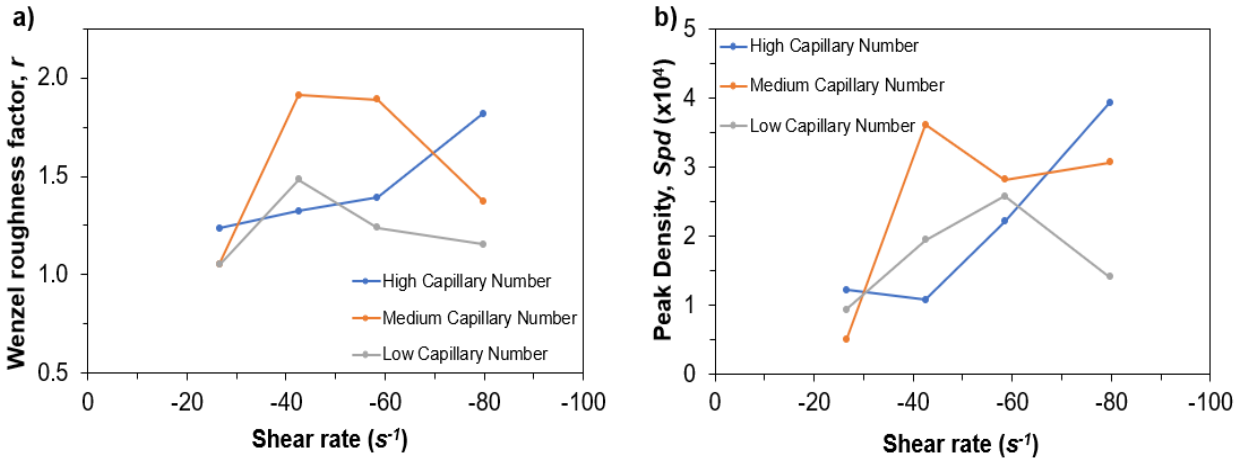

Figure 4.7: Variation of surface descriptors with respect to shear rate.

Figure 4.7 (a) show the variation of Wenzel roughness factor (r) with respect to the shear rate for various capillary numbers. It can be seen that the mid ca samples showed high r values. The samples with high Ca showed an increasing trend with respect to shear rate while the r value of the low and mid Ca samples increased initially and then decreased. The reason for this was attributed to the decrease in viscosity.

Similarly, Figure 4.7 (b) shows the variation of the peak density with respect to the shear rate for various capillary numbers. The low and mid Ca showed an initial increase and then a decrease in the peak density of the sample as the shear rate increased. The high Ca samples showed an increase in peak density as the shear rate increase. The sample with the highest shear rate (-79.80 s^{-1}) and the highest Ca (5.38 x 10^5) resulted with the highest peak density (3.94 x10^4 mm^{-2}).

4.7 Effect of Viscosity

The samples with high Ca showed an increasing trend with respect to shear rate while the r value of the low and mid Ca samples increased initially and then decreased. The reason for this was attributed to the decrease in viscosity. Since the paste is a shear thinning fluid, the viscosity was inversely proportional to the shear rate. As the shear rate increased, the viscosity kept reducing and when the shear rate crossed 60 s^{-1}, the viscosity became less than 9 x 10^4 Pa-s, the micro/nano structures couldn't hold itself since the material started to lose its elastic nature. Thus, 9 x 10^4 Pa-s is the limiting viscosity and the sample couldn't retain its micro/nano structure morphology beyond this point.

4.8 Water Contact Angle Results

The results from the water contact angle (WCA) experiment are reported in Table 4.3 and in Figure 4.8. Figure 4.8 (a) shows the statistical plot of the WCA of each sample. The sample 4a had the highest WCA while the sample 1c showed the lowest WCA. The Avg. WCA was plotted with respect to the shear rate and capillary number in Figure 4.9. This trend was very similar to the peak density and Wenzel roughness factor plots shows in Figure 4.6.

Since the superhydrophobicity depends on the peaks or textured surface of the sample, the WCA showed a very similar trend to the peak density plot showed in Figure 4.6 (b). Thus, this WCA results validated both the surface descriptor and SEM results and aided in identifying the optimum conditions to fabricate a superhydrophobic rough textured surface. From the WCA results, we found that for a high contact angle, the range of capillary number should be from 4.5 x 10^5 to 6.0 x 10^5 and shear rate should be from 40 s^{-1} to 60 s^{-1} similar to the surface descriptors. Almost all of the samples with capillary number around 5 x 10^5 and shear rate were greater than 40 s^{-1} (Sample 2b, 3b, 4a) had high WCA value.

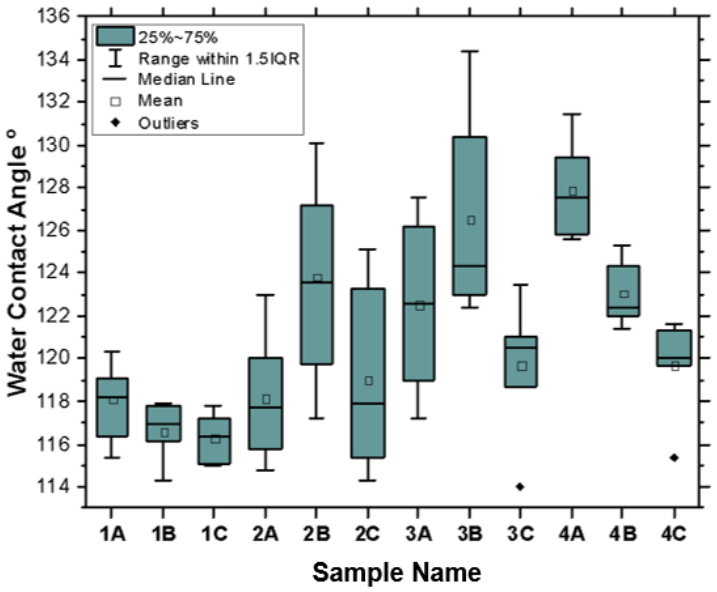

Figure 4.8: Water contact angle results.

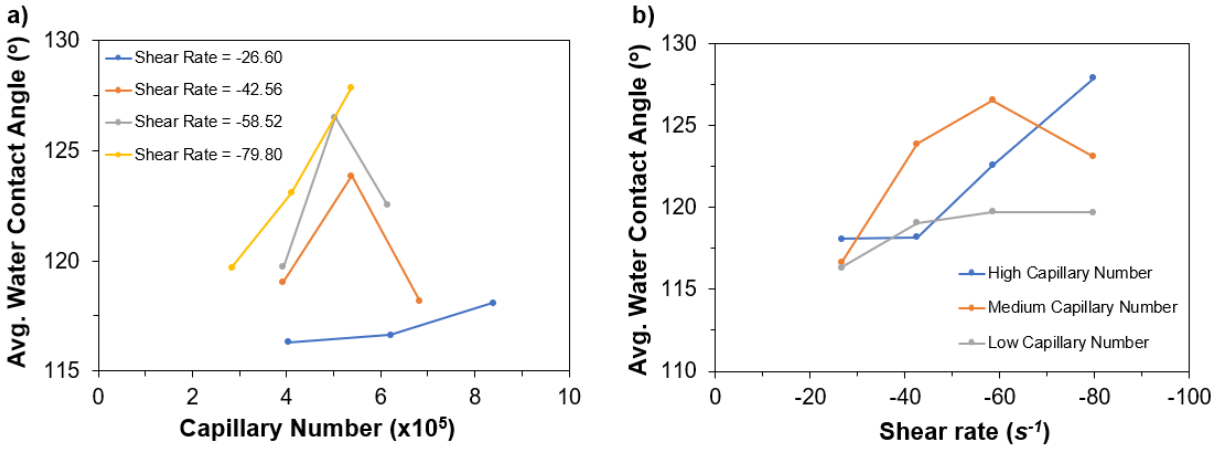

Figure 4.9: Variation of water contact angle with respect to capillary number and shear rate.

CHAPTER 5: CONCLUSIONS

Twelve samples with various shear rates and capillary numbers were fabricated using the roll coating. The SEM, surface roughness and the WCA for all these samples were analyzed to get insights on the optimum process condition to best mimic the bioinspired micro/nano textured rough surface. Thus, the critical factors involved in fabricating a rough textured surface was identified and reported through this study. The optimum regions of the capillary number and shear rate was found and reported.

The capillary number should be in the range of 4.5×10^5 to 6.0×10^5 and shear rate should be in the range of $40\ s^{-1}$ to $60\ s^{-1}$ for best bioinspired surfaces. Based on the SEM, surface descriptor and the WCA results we found that the samples 2b, 3a and 4a showed a high rough optimum surface texture similar to the bioinspired surfaces. The sample with high roughness and the textured surface was obtained with a shear rate of $-42.56\ s^{-1}$ and a capillary number of 5.38×10^5. All samples were hydrophobic in nature with a maximum WCA of 128^o. Thus, these two roll coating process parameters can be used to mimic the best bioinspired surfaces which can be used effectively in the super-hydrophobic, self-cleaning, anti-icing coatings, anti-biofouling, and drag reduction applications.

CHAPTER 6: FUTURE SCOPE

In the current study the two-roll coating process was effectively used to produce the random rough topography structures. All of the samples produced in the optimum processing conditions were hydrophobic in nature with a maximum WCA of 128^{o}.

The future target of this study is to use the two-roll coating process and the optimum parameters defined to produce linear regular topography surface which is superhydrophobic in nature with a WCA greater than 150^{o}.

The next steps in this direction will be as follows:

- A spherical nano particle can be used so the polymer composite will be without entanglement for uniformity of the coating surface.
- The nano particle wt % used can be varied to reach the optimum condition.
- A different curing methodology can be used to maintain a constant paste property.

REFERENCES

[1] C. Neinhuis, W. Barthlott, Characterization and distribution of water-repellent, self-cleaning plant surfaces, Ann. Bot. 79, 667–677 (1997).

[2] H. J. Ensikat, P. Ditsche-Kuru, C. Neinhuis, W. Barthlott, Superhydrophobicity in Perfection: the Outstanding Properties of the Lotus Leaf, Beilstein J. Nanotechnol, 2, 152−61 (2011).

[3] D. Byun, J. Hong, Saputra, J. H. Ko, Y. J. Lee, H. C. Park, B. K. Byun, J. R. Lukes, Wetting Characteristics of Insect Wing Surfaces, Journal of Bionic Engineering, 6, 63−70 (2009).

[4] B. Liu, Y. He, Y. Fan, X. Wang, Fabricating super-hydrophobic lotus-leaf-like surfaces through soft-lithographic imprinting, Macromol. Rapid Commun. 27, 1859–1864 (2006).

[5] R. J. Fields, M. F. Ashby, Finger-like crack growth in solids and liquids. Phil. Mag. 33, 33–48 (1976).

[6] P. H. Gaskell et al., J. Fluid Mech. (1998), vol. 355, 17-44

[7] E. Szczurek et al., Journal of materials processing technology, 20 (2009), 3187–3197

[8] C. H. Choi et al., Phys. Fluids 18, 087105 (2006)

[9] S. H. Park, S. Lee, D. Moreira, Bioinspired superhydrophobic surfaces, fabricated through simple and scalable roll-to-roll processing, Sci Rep 5, 15430 (2015).

[10] M. E. G. Castillo, A. T. Patera, Three-dimensional ribbing instability in symmetric forward-roll film-coating processes. J. Fluid Mech. 335, 323–359 (1997).

[11] C. D. Bandara, S. Singh, I. O. Afara, A. Wolff, T. Tesfamichael, K. Ostrikov, A. Oloyede, Bactericidal Effects of Natural Nanotopography of Dragonfly Wing on Escherichia coli, ACS Appl. Mater. Interfaces, 9, 6746−6760 (2017).

[12] D. E. Mainwaring, S. H. Nguyen, H. K. Webb, T. Jakubov, M. Tobin, R. Lamb, A. H. F. Wu, R. Marchant, R. J. Crawford, E. P. Ivanova, The Nature of Inherent Bactericidal

Activity: Insights from the Nanotopology of Three Species of Dragonfly, Nanoscale, 8, 6527−6534 (2016).

[13] Tong Wei et al., Journal of Inorganic Materials, 2019, 34(11): 1133-1144

[14] K.Y. Law, Highly Wettable Slippery Surfaces: Self-cleaning Effect and Mechanism, Int. Journ. of Wettability Science and Technology, Vol. 1, 31–45 (2018).

[15] James F. Schumacher, Michelle L. Carman, Thomas G. Estes, (2007): Engineered antifouling microtopographies – effect of feature size, geometry, and roughness on settlement of zoospores of the green alga Ulva , Biofouling: The Journal of Bioadhesion and Biofilm Research, 23:1, 55-62.

[16] J. Ou, B. Perot, J. P. Rothstein, Laminar drag reduction in microchannels using ultrahydrophobic surfaces, Phys. Fluids 16, 4635–4643 (2004).

[17] A. M. Grillet, A. G. Lee, E. S. G. Shaqfeh, Observations of ribbing instabilities in elastic fluid flows with gravity stabilization. J. Fluid Mech. 399, 49–83 (1999).

[18] Andrew Kozbial et al., *Langmuir 2014, 30, 28, 8598–8606 (2014).*